

Secondary bifurcation of mixed-cross-spirals connecting travelling wave solutions

This article has been downloaded from IOPscience. Please scroll down to see the full text article.

2010 New J. Phys. 12 113035

(<http://iopscience.iop.org/1367-2630/12/11/113035>)

View [the table of contents for this issue](#), or go to the [journal homepage](#) for more

Download details:

IP Address: 134.96.30.94

The article was downloaded on 19/11/2010 at 08:21

Please note that [terms and conditions apply](#).

Secondary bifurcation of mixed-cross-spirals connecting travelling wave solutions

S Altmeyer and Ch Hoffmann¹

Institut für Theoretische Physik, Universität des Saarlandes,
D-66123 Saarbrücken, Germany
E-mail: chhof@lusi.uni-sb.de and sepp@lusi.uni-sb.de

New Journal of Physics **12** (2010) 113035 (19pp)

Received 17 June 2010

Published 17 November 2010

Online at <http://www.njp.org/>

doi:10.1088/1367-2630/12/11/113035

Abstract. We present numerical results of secondarily forward bifurcating, stationary flow states that mediate transitions between travelling helical waves (spirals). These so-called mixed-cross-spirals (MCSs) can be seen as nonlinear superpositions of spiral solutions with different helicity and pitch. Thereby, the contribution of the respective spiral to the entire MCS varies continuously with the control parameters. Furthermore, MCSs connect the bifurcation branches of the involved spirals, even when both spiral pitches differ. This makes them interesting for pattern-forming systems in general. The bifurcation scenarios of MCSs differ from the well-studied cross-spiral-mediated transitions between mirror-symmetric left- and right-winding spirals, even in the case of MCS solutions that start and end in the *same* spiral branch.

The structure, spatiotemporal dynamics, bifurcation behaviour and stability of MCSs are elucidated in detail for the axially periodic Taylor–Couette system as a prototypical reference for pattern formation. The results are obtained by solving the full Navier–Stokes equations with a combination code of a finite differences and a Galerkin method.

 Online supplementary data available from stacks.iop.org/NJP/12/113035/mmedia

¹ Author to whom any correspondence should be addressed.

Contents

| | |
|---|-----------|
| 1. Introduction | 2 |
| 2. System and theoretical description | 3 |
| 2.1. Numerical methods | 4 |
| 2.2. Numerical analysis and visualization methods | 5 |
| 2.3. Spiral structure | 5 |
| 2.4. Ribbons and cross-spirals | 7 |
| 3. Structural properties | 7 |
| 3.1. Ribbons and mixed-ribbons | 7 |
| 3.2. Cross-spirals and mixed-cross-spirals | 8 |
| 3.3. Spatiotemporal properties | 9 |
| 4. Bifurcation and stability | 11 |
| 4.1. Frequencies | 15 |
| 4.2. Stability | 15 |
| 4.3. Phase diagrams | 16 |
| 5. Summary | 17 |
| Acknowledgment | 18 |
| References | 18 |

Nomenclature

We use the following abbreviations for the different flow states discussed in this paper:

| | |
|-------|-------------------------|
| CCF | circular Couette flow |
| TVF | Taylor vortex flow |
| SPI | spiral vortex flow |
| R-SPI | right-winding SPI |
| L-SPI | left-winding SPI |
| wTVF | wavy Taylor vortex flow |
| wSPI | wavy spiral vortex flow |
| CSPI | cross-spiral |
| RIB | ribbon |
| MCS | mixed-cross-spiral |
| MRIB | mixed-ribbon |

We denote R-SPIs with red triangles (\blacktriangledown , \triangledown), L-SPIs with orange triangles (\blacktriangle , \triangle), RIBs with green lozenges (\blacklozenge , \lozenge) and MCSs with maroon squares (\blacksquare , \square). Solid (dashed) lines with closed (open) symbols usually describe stable (unstable) solution branches or bifurcation thresholds of stable (unstable) states.

1. Introduction

The Taylor–Couette system consisting of a fluid between independently rotating cylinders is one of the most famous references for pattern-forming systems. Numerous structures with different

topology are known to appear in this system and have been studied extensively during recent decades. Experiments as well as numerical simulations [1]–[9] elucidate various solutions and bifurcation scenarios, in particular transitions between fully developed states.

The most important of these states² are the rotationally symmetric Taylor vortex flow (TVF) with toroidally closed vortices and the spiral vortex flow (SPI) with open, helicoidal vortices. Both bifurcate in primary forward bifurcations out of the basic state, i.e. circular Couette flow (CCF) [4]. Spirals occur as symmetry degenerated, oppositely travelling, right-winding (R-SPI) or left-winding spirals (L-SPI), being mirror images of each other [7, 10]. They are determined by their helicity and their azimuthal wave number M or, alternatively, by their pitch p . Depending on the control parameters, spirals with different slopes are observed, e.g. L1-SPIs or R2-SPIs. This notation is explained in section 2.3.

Besides this, more complex structures, such as axially standing waves, so-called ribbons (RIBs) and cross-spirals (CSPIs³), have been the subject of many detailed investigations [11]–[16]. Both can be seen as nonlinear superpositions of mirror-symmetric R- and L-SPIs with varying contributions and the *same* azimuthal wave number M . While SPIs and RIBs accrue at a common threshold, CSPIs bifurcate secondarily out of SPIs and connect them with the RIB branch.

Further secondarily bifurcating structures, namely the wavy Taylor vortices (wTVFs) and the wavy spirals (wSPIs) [13, 17]–[21], have been found to mediate the transitions between TVF and SPI, and typically exhibit a nonlinear superposition of R- and L-SPI modes with additional contributions from rotational symmetric components.

We have now found transitions between arbitrary SPI states, i.e. spirals with the *same* or with *different* pitches. Such processes are interesting for pattern-forming systems in general because they accomplish transitions between travelling waves of different azimuthal wave numbers and have not been described in the literature so far. We have identified a new class of solutions, so-called mixed-cross-spirals (MCSs), which mediate these transitions and were first observed in [22]. They can be seen as nonlinear superpositions of two SPI states with different helicity and different M but without the rotational symmetric contributions as in the wTVF or wSPI case. Thus, such transitions mainly involve the Fourier mode subspaces of the participating spiral structures. Furthermore, MCSs offer a way to connect the same or different SPI solution branches via secondary forward bifurcations.

This paper is roughly subdivided into three parts. After a short introduction (section 2) to the system and the numerical methods, section 3 compares the symmetry and spatiotemporal properties of numerically obtained CSPIs with MCSs. Section 4 then presents bifurcation, stability and phase diagrams elucidating different bifurcation scenarios, which have been found for MCSs.

2. System and theoretical description

We report numerically obtained results in the Taylor–Couette system (figure 1) with concentric, co- and counter-rotating cylinders, fixed radius ratio $\eta = r_1/r_2 = 0.883$, no-slip boundary conditions at the cylinder surfaces and axial periodic boundary conditions determining the axial wave number that is fixed in this paper to $k = 3.927$ ($\lambda = 1.6$). The fluid in the annulus between

² See the nomenclature.

³ We use here the abbreviation CSPIs for cross-spirals instead of the formerly used CR-SPIs.

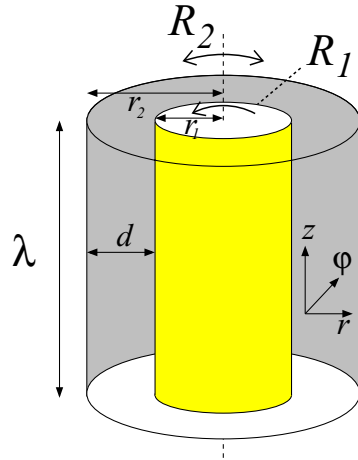


Figure 1. Geometry of the Taylor–Couette system. $r_{1,2}$ denote the inner and outer cylinder radii, λ is the periodicity length in units of $d = r_2 - r_1$ and $R_{1,2}$ are the respective inner and outer cylinder Reynolds numbers.

the cylinders (gap width $d = r_2 - r_1$) is considered to be isothermal and incompressible with kinematic viscosity ν .

Cylindrical coordinates r , φ , and z are used to decompose the velocity field into a radial component u , an azimuthal one v and an axial one w ,

$$\mathbf{u} = u \mathbf{e}_r + v \mathbf{e}_\varphi + w \mathbf{e}_z. \quad (1)$$

The system is governed by the Navier–Stokes equations,

$$\partial_t \mathbf{u} = \nabla^2 \mathbf{u} - (\mathbf{u} \cdot \nabla) \mathbf{u} - \nabla p. \quad (2)$$

Here, lengths are scaled by the gap width d and times by the radial diffusion time d^2/ν . The Reynolds numbers

$$R_1 = r_1 \Omega_1 d / \nu, \quad R_2 = r_2 \Omega_2 d / \nu \quad (3)$$

enter into the boundary conditions for v : R_1 and R_2 are just the reduced azimuthal velocities of the fluid at the cylinder surfaces, Ω_1 and Ω_2 are the respective angular velocities of the cylinders.

2.1. Numerical methods

Numerical simulations have been carried out with our ‘G2D2’ code, as presented in detail in [17]. G2D2 implements a Galerkin expansion in two dimensions, φ and z , and finite differences of second order in r and of first order in t ,

$$f(r, \varphi, z, t) = \sum_{m,n} f_{m,n}(r, t) e^{i(m\varphi + nkz)}, \quad f \in \{u, v, w, p\}. \quad (4)$$

Here, $f_{m,n}(r, t)$ are the amplitudes of the m th azimuthal and the n th axial Fourier mode. Their variation in the two variables r and t is determined using finite differences.

Note that the decomposition (4) of the velocity field allows one to impose restrictions on modes m and n and to enforce arbitrary symmetry conditions during the numerical calculations by selecting the subspace of the solution of interest. This makes it possible to follow the complete bifurcation branches of unstable as well as stable solutions.

2.2. Numerical analysis and visualization methods

For visualization purposes, we found the azimuthal vorticity component,

$$\Omega_\varphi = (\nabla \times \mathbf{u}) \cdot \mathbf{e}_\varphi = \partial_z u - \partial_r w, \quad (5)$$

to be an adequate and convenient means to identify and recognize the geometry of complex vortex structures via iso-vorticity surfaces. These so-obtained tubes represent the topology of vortex centres and thus determine the most important properties of the structures discussed here, e.g. symmetry, pitch and complexity. They further describe the strength of the vortices and give a rough impression of the vortex deformation, cf the $r - z$ vector plots of the velocity fields u and w on the left side in the movie (available from stacks.iop.org/NJP/12/113035/mmedia), which include the colour-coded azimuthal vorticity.

In order to classify the structures, we often refer to their significant Fourier mode indices abbreviated as (cf equation (4))

$$(m, n) := f_{m,n} e^{i(m\varphi + nkz)}, \quad f \in \{u, v, w, p\}. \quad (6)$$

2.3. Spiral structure

Since we deal in this paper extensively with spiral vortex flow as an ingredient in more complex structures, we briefly recapitulate the main spatiotemporal properties of spirals. Spiral vortex flow is periodic in time with oscillation frequency ω , periodic in z with wave number $k = 2\pi/\lambda$, and periodic in φ with wave number M . Furthermore, spiral vortices show a combined symmetry under rotation and axial translation or time translation, respectively: the spiral fields do not depend on φ, z, t separately but only on the phase combination [11]

$$\Phi := M\varphi + Kz - \omega t, \quad (7)$$

such that

$$f(r, \varphi, z, t) = F(r, \Phi). \quad (8)$$

The spiral frequencies ω depend on the Reynolds numbers $R_{1,2}$ and on the wave numbers M and K . The latter is given by $K = \pm k$, depending on the helicity of the respective spiral, i.e. $K > 0$ for L-SPI and $K < 0$ for R-SPI. R-SPI and L-SPI, characterized by $K = K_R, M = M_R, \omega = \omega_R$ and $K = K_L, M = M_L, \omega = \omega_L$, respectively, are mirror images of each other under the operation $z \rightarrow -z$, i.e.

$$\Phi_{\text{L-SPI}}(z, \varphi, t) = \Phi_{\text{R-SPI}}(-z, \varphi, t). \quad (9)$$

Considering various $M_{R,L} \geq 1$, this yields

$$K_L = -K_R, \quad M_L = M_R \quad \text{and} \quad \omega_L = \omega_R. \quad (10)$$

The frequencies are positive since the spirals rotate into the same direction as the inner cylinder. This in turn implies that the phase of an L-SPI propagates axially upwards while the converse holds for the R-SPI—the location $z_0(\varphi)$ of a particular phase value, say, $\Phi = 0$, at a fixed time t is given by

$$z_0 = -\frac{M}{K}\varphi + \frac{\omega}{K}t. \quad (11)$$

Thus, the reduced axial pitch p of an SPI can be defined as

$$p := \frac{z_0(2\pi) - z_0(0)}{\lambda} = -M \frac{k}{K} = -\text{sgn}(K) M, \quad (12)$$

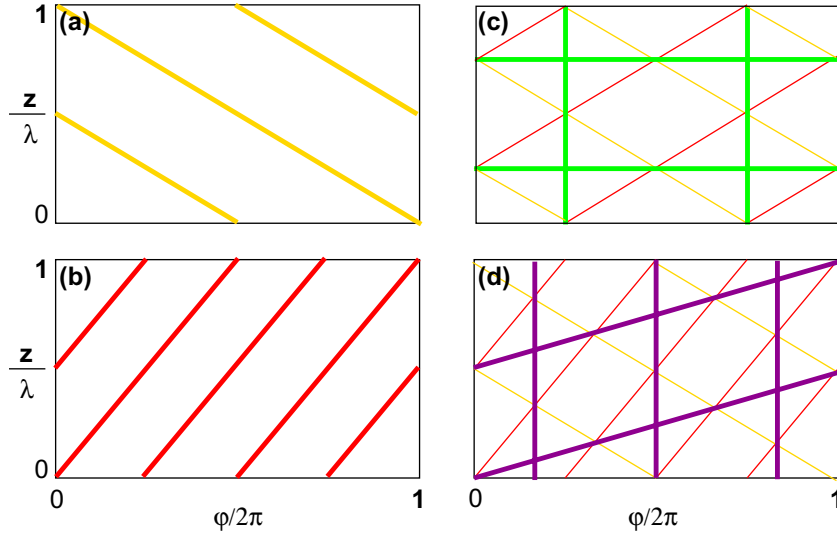


Figure 2. Characterization of different structures by lines of constant phase $\Phi = 0$ on an azimuthally unrolled cylindrical surface at mid-gap. (a) L1-SPI (orange) with pitch $p = -1$, (b) R2-SPI (red) with $p = 2$, (c) 1-RIB (green) with $p = 0$ composed of L1-SPI (orange) and R1-SPI (red), (d) L1R2-MRIB (maroon) with $p = 1/2$ composed of L1-SPI (orange) and R2-SPI (red) phase lines.

and gives the number of axial periodicity lengths being covered while travelling in the positive azimuthal direction along the helicoidal vortex tube once around the cylinder. Hence, $p\lambda/2\pi = -M/K$ is the slope of the lines of constant phase in the $\varphi - z$ plane of an azimuthally unrolled cylindrical surface.

In this paper, we consider only vortex structures with the same axial wave number $k = |K| = 3.927$, i.e. $\lambda = 1.6$. We identify the different spirals investigated here by the following combination of letters and numbers: e.g. L1-SPI is a left-winding spiral with azimuthal wave number $M = 1$ (thus $p = -1$) while R2-SPI stands for an R-SPI with azimuthal wave number $M = 2$ (thus $p = 2$), cf figure 2. The symbols L1 and R2 correspond to the pitch of the SPI. Furthermore, the pitch of a TVF structure vanishes, i.e. $p = 0$.

Primary forward bifurcating TVF and SPI are usually characterized by a few dominant azimuthal and axial modes (m, n) , cf equation (6). Apart from higher harmonics, TVF is mainly determined by the mode $C \equiv (0, 1)$ and its complex conjugate $\bar{C} \equiv (0, -1)$. On the other hand, the right-winding R1-SPIs (left-winding L1-SPIs) with azimuthal wave number $M = 1$ are characterized by $A \equiv (1, -1)$ and $\bar{A} \equiv (-1, 1)$ [$B \equiv (1, 1)$ and $\bar{B} \equiv (-1, -1)$], cf [17].

Because of the symmetry equation (7) of the spiral vortex structure, the azimuthal and axial Fourier mode indices m and n of the decomposition equation (4) then satisfy $m = -pn$ for these structures. Thus, spirals with the pitch p live in the $(-pn, n)$ diagonal subspace of the (m, n) Fourier mode space, where $n \in \mathbb{Z}$, cf [9]. On the other hand, TVFs with $p = 0$ lives in the $(0, n)$ subspace. RIB structures exhibit the same pitch $p = 0$ as TVFs, but they live in a combined subspace $(0, n) \oplus (\pm p_{\text{SPI}}n, n)$ with p_{SPI} being the pitch of the corresponding spiral (cf. below). All these subspaces are spanned by the characterizing modes A , B and C of the respective structure.

2.4. Ribbons and cross-spirals

RIBs bifurcate together with spirals at a common threshold. They can be seen as nonlinear superpositions of mirror-symmetric R-SPI and L-SPI modes with equal amplitudes $A = B$. Thus, in the case of $M = 1$ spirals, 1-RIBs are characterized by identical contributions from the modes $A \equiv (1, -1)$ and $B \equiv (1, 1)$ and a weaker contribution of their nonlinear combination $C \equiv (0, 2)$. Analogously, 2-RIBs are determined by the dominant $(2, 1)$, $(2, -1)$ and $(0, 2)$ modes.

SPI and RIB solution branches are connected by secondarily bifurcating cross-spirals (CSPIs). They are generally described by the same modes A , B and C , which then, however, are different, e.g. near the SPI branch, one of A or B is significantly larger than the other, which even vanishes at the bifurcation point.

Common to RIBs and CSPIs is that they only occur as superpositions of an R- and an L-SPI with the *same* azimuthal wave number M . This no longer applies for mixed-ribbons and mixed-cross-spirals.

3. Structural properties

MCSs can be seen as nonlinear superpositions of two spirals with different helicity and different azimuthal wave numbers $M_1 \neq M_2$, i.e. their pitches satisfy $\text{sgn}(p_1 p_2) = -1$. Depending on the amplitude ratio of the dominant spiral components, $|u_R|/|u_L| = A/B$, one finds either ribbon-like (mixed-ribbons, MRIBs) or open, helicoidal MCSs. The latter bifurcate secondarily out of an SPI branch and live in a mode subspace given by a nonlinear superposition of the linear mode subspaces spanned by $\bar{A} \equiv (-p_1, 1)$ and $B \equiv (-p_2, 1)$, respectively—cf equation (12).

In general, MCSs occur in a broad parameter range and connect any type of spiral solution branches, i.e. spirals with the *same* or with *different* pitches. Throughout this paper, we present MCSs that only exist for control parameters where at least two spiral types with different azimuthal wave numbers coexist simultaneously. Furthermore, we focus on the special case of bifurcation start and end points in the *same* SPI branch.

In this section, we discuss the classification and basic symmetry properties of MCSs and MRIBs, and compare them with the ‘classical’ CSPIs and RIBs. As mentioned above, the latter can be seen as nonlinear superpositions of spirals with different helicity but the *same* azimuthal wave numbers $M_1 = M_2$ and are extensively studied in [11]–[14]. An intuitive access to the structural properties of CSPIs, RIBs, MCSs and MRIBs is offered by investigating the linear superpositions of their significant Fourier modes. Fully developed MCS states (obtained by numerical simulations of the full Navier–Stokes equations (2)) will then be treated in the subsequent sections.

3.1. Ribbons and mixed-ribbons

Figure 2 illustrates the symmetry of L1-SPIs (a) and R2-SPIs (b), represented by one significant Fourier mode, respectively. The (green) $\Phi = 0$ phase lines of the linear 1-RIB (c) can be seen as a linear superposition of the (orange) L1-SPI with $p_1 = -1$ and the (red) R1-SPI with $p_2 = 1$. Analogously, the $p_1 = -1$ and $p_2 = 2$ structures superimpose to (maroon) MRIB (d). In contrast to figure 2(c) of a regular ribbon pattern, figure 2(d) visualizes the displaced chequerboard pattern caused by different slopes of the contributing spiral components.

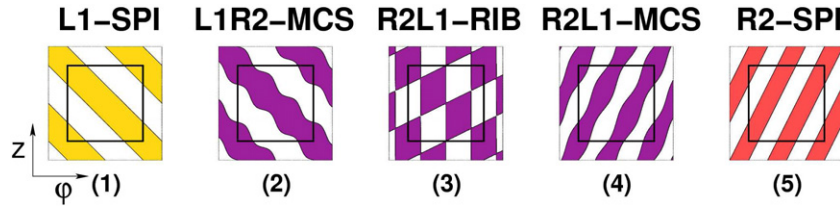


Figure 3. Schematic illustrations of MCSs (maroon) with different contributions from L1-SPI (orange) and R2-SPI (red). The amplitude ratio $\delta := |u_{R2}|/|u_{L1}|$ increases from $\delta = 0$ (L1-SPI), $\delta = 0.5$ (L1R2-MCS), $\delta = 1$ (L1R2-MRIB), $\delta = 2$ (R2L1-MCS) and $\delta = \infty$ (R2-SPI) from left to right. The coloured regions denote radial outflow, $u > 0$, and the white ones indicate radial inflow, $u < 0$, in the plane of an unrolled cylinder surface in the annulus. The inner squares cover the azimuthal period 2π in the horizontal direction and one axial wavelength λ in the vertical direction. For better visibility, the structures are periodically continued slightly beyond these limits.

In the following, we use a notation that reflects both dominant components in an MCS or MRIB. For example, in figure 2(d), the L1 and R2 contributions combine to an L1R2-MRIB or, in the case of unequal contributions, to an L1R2-MCS.

In contrast to 1-RIBs with vertical and horizontal phase lines, i.e. with pitch $p = 0$, L1R2-MRIBs consist of vertical as well as azimuthally increasing or decreasing phase lines, i.e. with $p \neq 0$. Obviously, equal contributions from spirals with different helicities, i.e. $\text{sgn}(p_1 p_2) = -1$, superimpose to an RIB or MRIB pattern with $|p_1 - p_2|$ vertical $\Phi = 0$ lines and the pitch $p = (p_1 + p_2)/2$. Note that, in general, the value of the azimuthal wave number $M = |p|$ of an arbitrary vortex structure is always half the number of zeros of Φ in the azimuthal direction.

3.2. Cross-spirals and mixed-cross-spirals

In figures 2(c) and (d), the dominant components go into the 1-RIB and the L1R2-MRIB structure with the same amplitude, respectively (causing the eye-catching chequerboard patterns). As in the case of CSPIs, in the fully developed MCS structure, one of both spiral components (which we will refer to as the major component) usually dominates the other one (minor component). This is also reflected by our notation, e.g. ‘R2L1-MCS’ (‘L1R2-MCS’) indicates a major R2-SPI (L1-SPI) and a minor L1-SPI (R2-SPI) contribution to the complete Fourier spectrum of the MCS. However, a difference in the contributing amplitudes breaks the chequerboard symmetry and an open, helical structure appears with a slope defined by the major spiral component and a modulation caused by the minor one.

A schematic illustration in figure 3 of a linear superposition of $p_1 = -1$ and $p_2 = 2$ spiral contributions with varying amplitude ratio elucidates the symmetry of MCSs and MRIBs. Starting in (1) with a pure L1-SPI and increasing the R2 component first leads to a left-winding L1R2-MCS (2) with the azimuthal wave number $M = 1$ and the pitch $p = -1$. Equal L1 and R2 contributions in (3) yield L1R2-MRIB (as in figure 2(d)) with $p = 1/2$. In (4), the dominant R2 contribution of an R2-SPI establishes the right-winding character of an R2L1-MCS, finally followed in (5) by a pure R2-SPI with a vanishing L1 component.

The spatiotemporal behaviour of MCSs exhibits aspects of both, SPIs and RIBs. Usually, all (vertical and horizontal) $\Phi = 0$ phase lines rotate in the same direction as the inner cylinder.

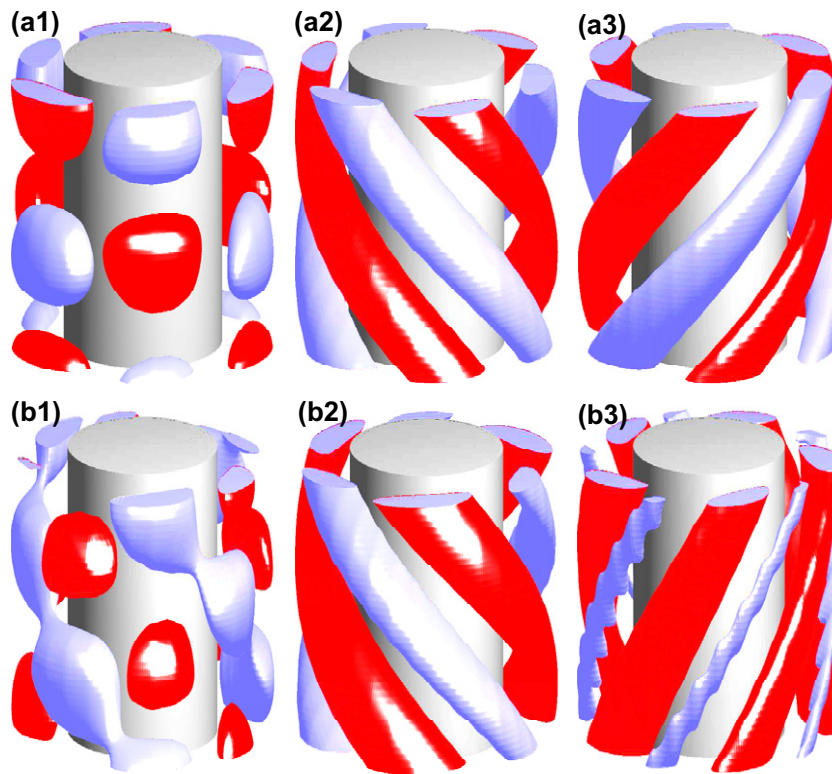


Figure 4. Iso-surfaces of azimuthal vorticity Ω_ϕ of numerically calculated (a) 3-RIB and (b) L3R5-MCS at $R_1 = 200$, $R_2 = 0$ (cross in the phase diagram of figure 7(d2)). In the axial direction, each plot covers one axial wavelength λ . The first column displays the complete structure. The second and third columns depict the separated contributions of the respective L-SPI and R-SPI components, namely the $(3n, n) \hat{=} L3$ (a2), $(-3n, n) \hat{=} R3$ (a3), $(3n, n) \hat{=} L3$ (b2) and $(-5n, n) \hat{=} R5$ (b3) subspaces, as illustrated in figure 5. Red (blue) indicates positive (negative) iso-vorticity values as listed in table 1, which also includes the respective vorticity maxima and minima.

The horizontal phase lines of RIBs are pinned at distinct $z = \text{const}$ positions. This no longer holds for MRIBs, cf figure 2(d). Here, the phase lines propagate axially due to their finite slope and the rotation of the entire pattern. Thus, the axial propagation direction of the open, fully developed MCS structures in figure 3 is determined by the major spiral contribution (here L1), while the modulation generated by the minor one (here R2) travels in the opposite direction (movie available from stacks.iop.org/NJP/12/113035/mmedia). This is completely analogous to the situation of CSPIs [11].

Note that CSPIs (RIBs) represent a special type of MCS (MRIB). On the other hand, RIBs (MRIBs) can be seen as a special type of CSPI (MCS) with equal amplitude contributions from L-SPIs and R-SPIs.

3.3. Spatiotemporal properties

In order to get an impression of the spatial shape of MCSs obtained by numerical simulations of the full Navier–Stokes equations, figure 4 compares the iso-vorticity surface plots of a 3-RIB

Table 1. Iso-vorticity values of figure 4.

| Plot | Lin. subspace | min Ω_φ | max Ω_φ | Iso- Ω_φ | Iso/min (%) | Iso/max (%) |
|------|----------------|----------------------|----------------------|-----------------------|-------------|-------------|
| (a1) | $L3 \oplus R3$ | -68 | 68 | ± 40 | 58 | 58 |
| (a2) | L3 | -35 | 35 | ± 20 | 56 | 56 |
| (a3) | R3 | -35 | 35 | ± 20 | 56 | 56 |
| (b1) | $L3 \oplus R5$ | -173 | 143 | ± 70 | 40 | 49 |
| (b2) | L3 | -93 | 121 | ± 60 | 64 | 49 |
| (b3) | R5 | -35 | 64 | ± 33 | 92 | 51 |

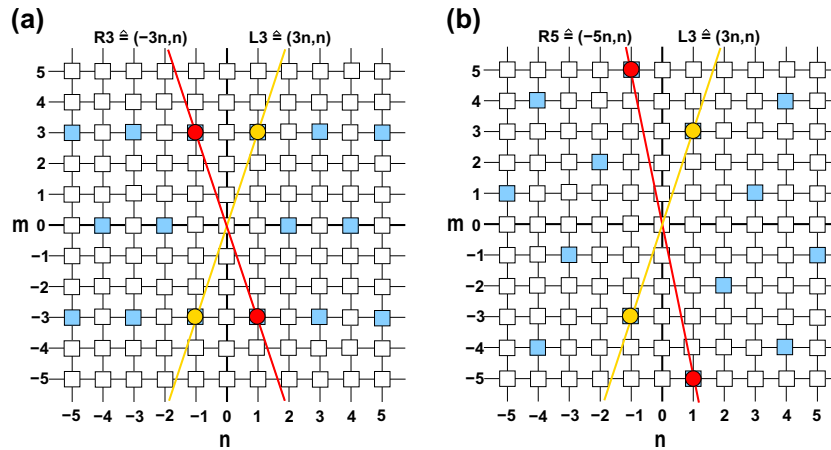


Figure 5. Excited modes (blue squares) of the (a) 3-RIB and (b) L3R5-MCS of figure 4 in the two-dimensional Fourier mode space spanned by the azimuthal and axial Fourier mode indices m and n . Blue squares with red or orange circles denote linearly driven modes and respectively superimpose to linear Fourier mode subspaces indicated by thick lines. They represent linear R3-SPI $(-3n, n)$, L3-SPI $(3n, n)$ in panel (a) and linear R5-SPI $(-5n, n)$, 3-SPI $(3n, n)$ in panel (b). Blue squares without a circle indicate nonlinearly driven modes.

(a1) with an L3R5-MCS (b1) at $R_1 = 200$ and $R_2 = 0$ under periodic boundary conditions. The iso-vorticity values for all plots are chosen to lie near the half of the respective global maximum of the azimuthal vorticity (table 1). The second and the third column contain separate contributions from the respective linear R- and L-SPI Fourier subspaces, i.e. $(3n, n)$ (a2) and $(-3n, n)$ (a3), as well as $(3n, n)$ (b2) and $(-5n, n)$ (b3). The corresponding linear subspaces are illustrated in figure 5 by thick lines, which connect the linearly driven modes of the respective subspace. The nonlinearly driven modes are indicated by blue squares without circles.

Obviously, both mirror-symmetric right- and left-winding spiral components represent the main contributions to the total vorticity of the 3-RIB solution in figures 4(a1)–(a3). Nonlinearly driven modes, which lie outside the diagonal $(\pm 3n, n)$ Fourier subspaces, play only a minor role in its mode spectrum. The vorticities in the respective components of figures 4(a2) and (a3) are in general slightly smaller than those of the entire structure in figure 4(a1), as described by the maximum values listed in table 1.

On the other hand, the L3R5-MCS in figure 4(b1) consists of a stronger L3 in figure 4(b2) and a weaker R5 component in figure 4(b3). Both component plots depict the iso-surface for a vorticity value of about 50% of the respective maximum. However, the vorticity maxima

in figures 4(b2) and (b3), and therefore also their contributions to the entire structure, differ significantly, so that the L3 contribution dominates the whole L3R5-MCS structure and the R5 portion only generates a weak modulation. In this case, the entire structure propagates upwards, i.e. in the positive axial direction, due to the major L3 component, whereas the modulation travels downwards.

It is remarkable that the blue vortex tubes of counterclockwise (while looking into the positive φ direction)-rotating vortices in figure 4(b3) are significantly smaller than the red, clockwise-rotating ones. Since, in general, the vorticity is strongest along a distinct line in the interior of a vorticity tube, the absolute maximum of the vorticity inside the larger red tubes is greater than that in the smaller blue ones. Furthermore, the vorticity is positive (negative) in the red (blue) vortex; thus $|\min \Omega_\varphi| < |\max \Omega_\varphi|$, cf table 1. Probably, this is a consequence of the non-vanishing intrinsic axial net flow generated by both spiral components (cf [10]) that influences clockwise- and counterclockwise-rotating vortices in different ways. In the case of ribbons, there is no axial net flow due to the equal contributions from both spiral types and therefore no remarkable difference in ‘red’ and ‘blue’ vortices (table 1).

Figure 6 elucidates for moderate driving ($R_1 = 200$, $R_2 = 0$) different spatial properties of L3R4-MCS (4), L3R5-MCS (5) and L4R5-MCS (6) and compares them with different RIB solutions, namely 3-RIB (1), 4-RIB (2) and 5-RIB (3). All these states coexist simultaneously. On the other hand, we found neither stable nor unstable CSPIs for the chosen control parameters.

Figure 6(a) contains iso-surface plots of the azimuthal vorticity for these six structures with iso-vorticity values of about 40–60% of the respective vorticity maximum (table 2). The corresponding Fourier mode spectra are depicted in figure 6(b). Although the calculations were performed with $n_{\max} = m_{\max} = 15$ in order to include at least three significant modes of the linear Fourier subspaces $(\pm 3n, n)$, $(\pm 4n, n)$ and $(\pm 5n, n)$, we only present, for the sake of visibility, a smaller cut-out, containing only the dominant modes. Figure 6(c) depicts grey-coded plots of the radial velocity $u(\varphi, z)$ on an unrolled cylindrical $\varphi - z$ surface at mid-gap, as well as the respective lines of constant phase (cf figure 2) of both spiral components. Finally, figure 6(d) gives vector plots of radial and axial velocity (u, w) in an $r - z$, plane including the colour-coded azimuthal vorticity.

All structures are stationary and rotate as a whole in the positive azimuthal direction. The RIB structures in figures 6(c1)–(c3) exhibit the typical chequerboard symmetry of an axially non-propagating, i.e. standing and azimuthally propagating, wave. However, with increasing M , their vortex centres slightly move towards the outer cylinder and the maximal vorticity also increases in figures 6(d1)–(d3).

In contrast to that, MCS structures propagate in the axial direction of the major component (figures 6(b4)–(b6)) and exhibit a helicoidal shape with a modulation (figures 6(c4)–(c6) and (a4)–(a6)) travelling into the opposite direction. The vector plots in figure 6(d) were taken at a distinct φ position where the phases of all structures coincide. Obviously, the L4R5-MCS in figure 6(d6) and the L3R4-MCS in figure 6(d4) are very similar and differ from the L3R5-MCS in figure 6(d5). Probably, this is only a geometric effect caused by the higher difference in the slopes of the participating L3-SPI and R5-SPI of figure 6(d5).

4. Bifurcation and stability

As mentioned above, MCSs bifurcate secondarily in a forward Hopf bifurcation out of pure spirals. In this paper, we only present MCSs existing for control parameters where at least two

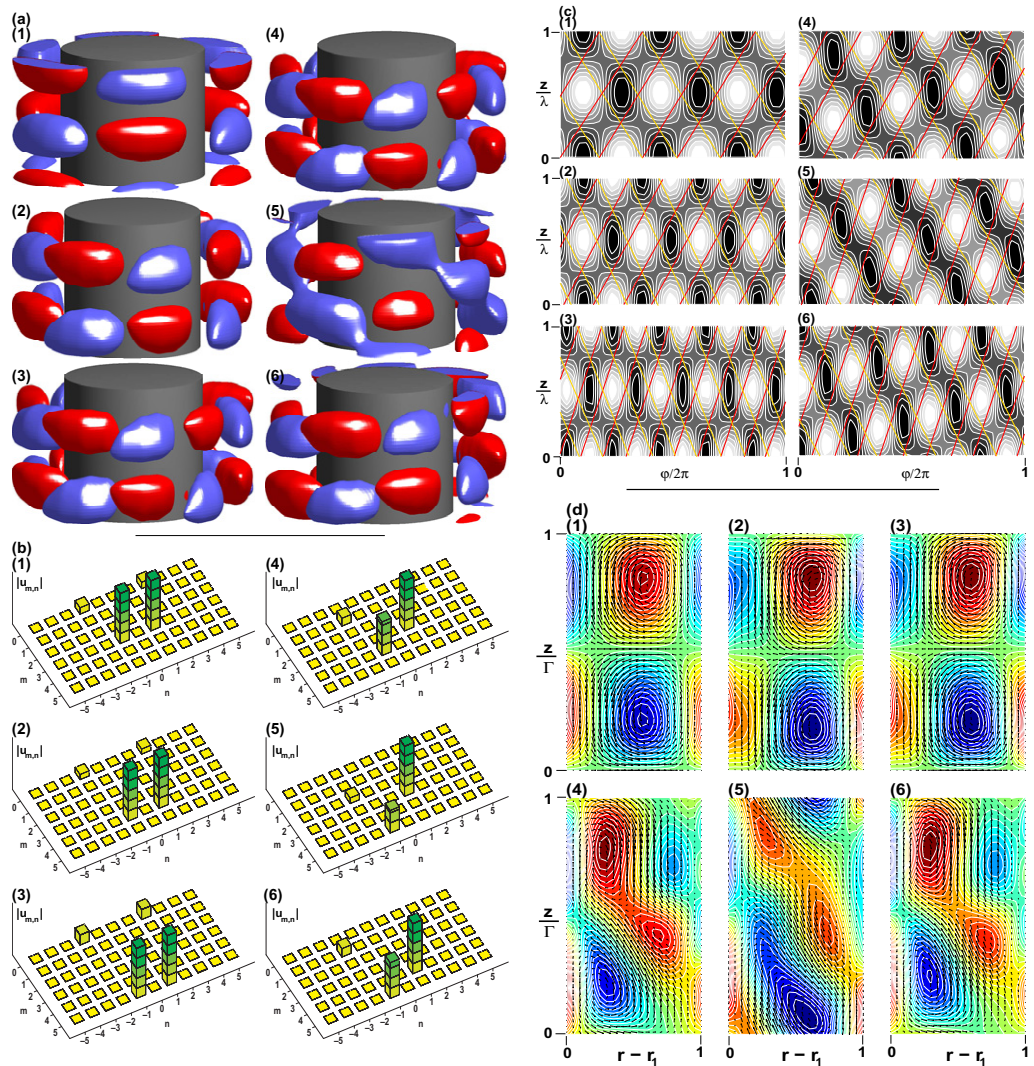


Figure 6. Comparison of numerically calculated, fully developed (1) 3-RIB, (2) 4-RIB and (3) 5-RIB with (4) L3R4-MCS, (5) L3R5-MCS and (6) L4R5-MCS. (a) Iso-surfaces of the azimuthal vorticity Ω_φ . Red (blue) indicates positive (negative) iso-vorticity values, as listed in table 2, including the respective vorticity minima and maxima. Each plot covers an axial periodicity length λ . (b) Mode amplitudes $|u_{m,n}|$ of the radial velocity field u for the azimuthal and axial Fourier mode indices, m and n , in a cut-out of the complete Fourier space. (c) Grey-coded radial velocity $u(\varphi, z)$ on an unrolled cylindrical surface in the annulus at mid-gap. Black (white) denotes maximal inflow (outflow). Orange and red lines denote the phase lines of the respective pure spiral components and are included to guide the eye. (d) Vector plots $(u(r, z), w(r, z))$ of the radial and axial velocity component in a $\varphi = \text{const}$ plane, including the azimuthal vorticity colour coded from blue (minimum) to red (maximum). Control parameters for all plots: $R_1 = 200$, $R_2 = 0$.

Table 2. Iso-vorticity values of figure 6(a).

| Plot | Lin. structure | min Ω_φ | max Ω_φ | Iso- Ω_φ | Iso/min (%) | Iso/max (%) |
|------|----------------|----------------------|----------------------|-----------------------|-------------|-------------|
| (1) | 3-RIB | -68 | 68 | ± 40 | 58 | 58 |
| (2) | 4-RIB | -158 | 166 | ± 60 | 38 | 36 |
| (3) | 5-RIB | -153 | 157 | ± 60 | 39 | 38 |
| (4) | L3R5-MCS | -173 | 143 | ± 70 | 40 | 49 |
| (5) | L4R5-MCS | -150 | 168 | ± 75 | 50 | 45 |
| (6) | L3R4-MCS | -159 | 174 | ± 75 | 47 | 43 |

spiral solutions with different helicities and pitches p_1 and p_2 , i.e. $\text{sgn}(p_1 p_2) = -1$, coexist simultaneously. However, this is not a necessary condition for MCSs to accrue: we also found MCS branches that at least partly lie within regions where only the spiral type exists, which corresponds to the major spiral component of the MCS.

For the outer cylinder at rest, figures 7(a)–(c) depict, depending on R_1 and R_2 , the bifurcation diagrams for amplitudes and frequencies of the structures discussed in the previous section. R_1 and R_2 vary in the range indicated by the arrows labelled with α , β and γ in the phase diagram of figure 7(d).

L3-SPI and L4-SPI as well as the respective RIB solutions bifurcate primarily as unstable solutions out of CCFs in figure 7(a) and may become stable for distinct control parameters. While increasing R_1 , further primary bifurcations of R4-SPI and R5-SPI, including the respective RIBs, arise as unstable solutions. At even larger R_1 , in the grey-marked regions, L3R4-MCS (1), L3R5-MCS (2) and L4R5-MCS (3) branch out of the L3-SPI (1,2) and L4-SPI (3), respectively—described (according to equation (6)) by the respective dominant (major and minor) modes $(m, n) = (3, 1)$ and $(4, -1)$ in figure 7(1), $(3, 1)$ and $(5, -1)$ in figure 7(2), as well as $(4, 1)$ and $(5, -1)$ in figure 7(3).

Due to the absence of axial symmetry breaking effects, left- and right-winding SPI solutions are degenerated, i.e. L- and R-SPIs with different helicity but the same azimuthal wave number bifurcate at the same common threshold. This also holds for MCS states, e.g. L3R4-MCS and its mirror image R3L4-MCS. In the following, we restrict our presentation to only one of both mirror-symmetric MCS solutions and to those SPI types that correspond to the respective MCS components. Furthermore, solutions with smaller $M \leq 2$ are not of interest here and are therefore not shown in the figures.

Obviously, MCSs always bifurcate out of that spiral solution with the larger amplitude. At the onset, the amplitude of the respective MCS component equals the respective SPI amplitude whereas the other component's amplitude starts from zero. There seems to be no simple correlation between the positions of the SPI and MCS onsets.

Finally, while increasing the control parameter beyond $R_1 \approx 250$, the structures discussed here become unstable against more complex or turbulent states.

Complete MCS branches, as shown in figure 7(c), can be obtained by holding R_1 fixed and varying R_2 in the range indicated by the arrows β and γ in the phase diagrams of figure 7(d). For example, the L3R5-MCS of figure 7(c2) with $R_1 = 200$, represented by modes $(3, 1)$ and $(5, -1)$, bifurcate secondarily as unstable solutions out of unstable L3-SPI within the grey marked area, which, as described above, lies completely inside the region where *both* spirals, L3-SPI and R5-SPI, exist simultaneously.

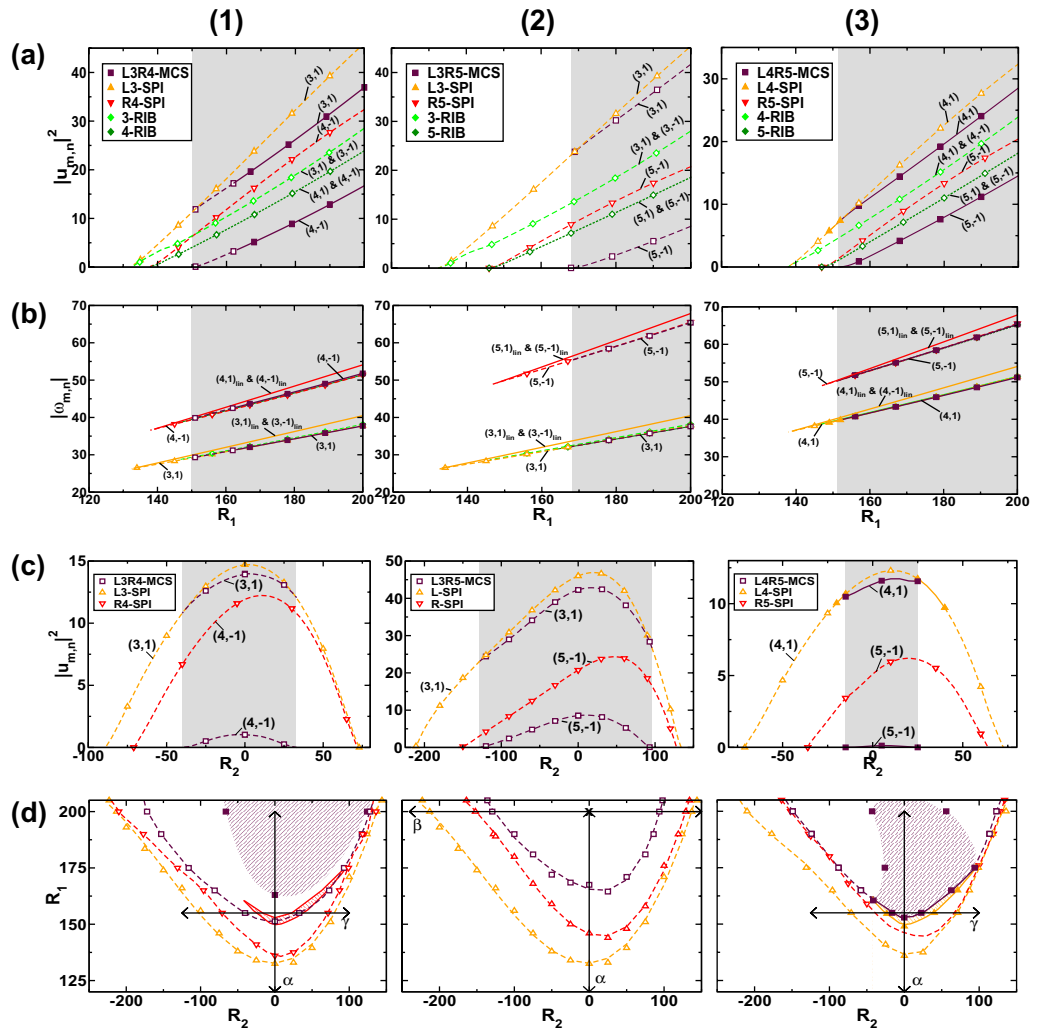


Figure 7. Comparison of different numerically obtained MCS and SPI solutions: (1) L3R4-MCS (■, □) bifurcating out of L3-SPI (▲, △), (2) L3R5-MCS (■, □) bifurcating out of L3-SPI (▲, △) and (3) L4R5-MCS (■, □) bifurcating out of L4-SPI (▲, △), as well as R-SPIs (▼, ▽), and RIBs (◆, ◇). Solid (dashed) lines denote stable (unstable) states or approximate bifurcation thresholds of stable (unstable) solutions. (a) Bifurcation diagrams of the radial velocity amplitude $|u_{m,n}|^2$ and (b) corresponding frequencies $|\omega_{m,n}|$ of the respective dominant modes (cf equation (6)) with R_1 varying along the arrows labelled with α in (d). Thin lines (thick lines with symbols) represent linear (nonlinear) frequencies obtained by a shooting method (full simulations). For MCSs, we captured both the major and the minor mode components, e.g. (3, 1) and (4, -1) for L3R4-MCS and analogously for the other MCSs. (c) Bifurcation diagrams with R_2 varying along the arrows labelled β and γ in (d). (d) Phase diagrams with closed (open) symbols and solid (dashed) approximating lines representing bifurcation thresholds of stable (unstable) solutions. The hatched areas in (1)–(3) roughly describe regions of stable MCSs (maroon in (d1) and (d3)), stable R4-SPI (red in (d1)) and stable L4-SPI (orange in (d3)).

For a smaller $R_1 = 155$, L3R4-MCS in figure 7(c1) and L4R5-MCS in figure 7(c3) bifurcate analogously out of L3-SPI and L4-SPI, respectively. Depending on the control parameter driving, different types of stability transfer are observed and will be discussed in section 4.2.

4.1. Frequencies

In figure 7(b), the frequencies of MCSs are compared with those of nonlinear and linear SPIs. SPIs and RIBs with $M \geq 3$ emerge via a primary Hopf bifurcation with the same, non-vanishing frequency that increases almost linearly with R_1 . This is different from SPIs and RIBs for $\eta = 0.5$ and $M < 2$, for which we found decreasing (increasing) frequencies near (far from) the onset (cf [10]). Thus, for the large η chosen here, linear and nonlinear SPI frequencies behave almost identically.

MCSs are time-periodic, rotating and axially propagating states. In the parameter range discovered here, the frequencies of both dominant spiral components of all MCS structures coincide very well with the respective frequencies of the corresponding pure spiral solutions. The contribution from the nonlinearly driven modes is small enough so that the spatiotemporal behaviour of MCSs is mainly determined by a linear superposition of both dominant mode frequencies. This represents a significant difference from other secondarily bifurcating structures, such as wavy spirals (cf [17]).

As shown exemplarily in the movie (available from stacks.iop.org/NJP/12/113035/mmedia) of an L3R5-MCS, the spatiotemporal behaviour is characterized by the axial propagation of the vortices, determined by the major spiral component, and an oppositely travelling modulation of the vortices, caused by the minor spiral component. The movie illustrates the transition from L3-SPI as the initial state to an L3R5-MCS by instantaneously jumping to the appropriate control parameters ($R_1 = 200$, $R_2 = 0$) after starting with noise in all modes. On the left, vector plots of the velocity fields (u , w) and colour-coded azimuthal vorticity (blue=minimum, red=maximum and thick black line $\Omega_\phi = 0$) are shown (cf figure 6(d)).

In the middle, the grey-coded radial velocity field $|u(\phi, z)|$ is plotted on an unrolled cylindrical surface at mid-gap (cf figure 6(c)). Here, black (white) represents inflow (outflow) regions and the thick red lines of $u = 0$ give a good guide for the position of the vortex centres.

The first 40 frames show the upward propagating L3-SPI. In the following frames, the influence of the R5-SPI contribution grows continuously, as indicated by the increasing modulation of the iso-lines in the $\phi - z$ plot. This modulation generates localized amplifications or attenuations of the in- and outflow amplitudes, represented by the occurrence of new, closed iso-lines in frames 150–270. At about frame 270, a fully developed L3R5-MCS propagates upwards (major L3 contribution) with a downwards travelling modulation (minor R5 contribution).

4.2. Stability

As described in [7, 10], SPIs with $p = \pm 1$ bifurcate for moderate outer cylinder rotation (and periodic boundary conditions) as unstable solutions out of CCFs and become stable for larger R_1 . This is also valid for SPIs and even for RIBs with $|p| > 1$, especially for the spirals investigated here: 3-SPI, 4-SPI and 5-SPI. MCS can bifurcate either as a stable or as an unstable

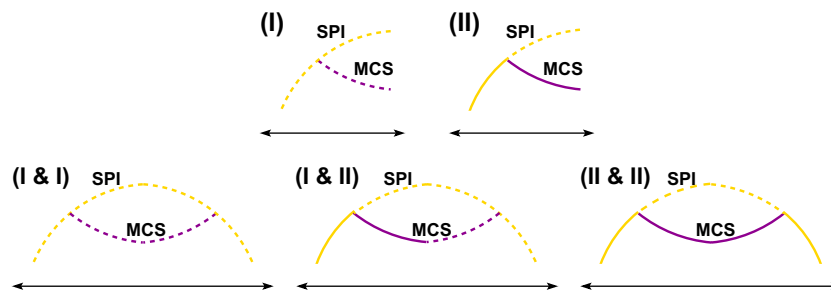


Figure 8. Schematic illustration (for a suitable control parameter in the parameter range covered in figure 7(d)) of the bifurcation scenarios (I) and (II) and their combinations near the MCS bifurcation thresholds. Solid (dashed) lines represent stable (unstable) solutions.

solution out of a SPI branch. The stability behaviour is indicated by solid and dashed lines in figure 7. Two scenarios are observed:

- An unstable MCS bifurcates out of an unstable SPI branch. The latter thereby does not change its stability. This is the case for the L3R4- and the L3R5-MCS in figures 7(a1) and (a2), as well as for both bifurcation points in figures 7(c1) and (c2).
- A stable MCS bifurcates out of a stable SPI solution that then becomes unstable. This is the case for the L4R5-MCS in figure 7(a3) and for both bifurcation points in figure 7(c3).

We found MCS branches exhibiting both bifurcation types and their three combinations that are schematically depicted in figure 8. As shown in the following section, a distinct MCS may change its stability depending on the control parameter driving in R_1 and R_2 .

For the control parameters chosen here, both spiral solutions that correspond to the dominant spiral components in the MCS structure coexist simultaneously with the respective MCS. But only that SPI corresponding to the *major* spiral component in the MCS state is able to interchange stability with the MCS. In other words, the stability transfer is not affected by the stability behaviour of that SPI corresponding to the *minor* spiral component. Therefore, these SPI branches are omitted in figure 8. Finally, the RIB solutions presented here are unstable within the entire parameter range covered in this paper.

We would like to stress that both scenarios describe only the stability in the vicinity of the bifurcation points and do not predict the stability properties farther away. In fact, we found rather complex stability behaviour: e.g. the L4R5-MCSs in figure 7(c3) bifurcate as a stable solution out of an L4-SPI that is stable just before the bifurcation point and loses its stability, just behind it.

4.3. Phase diagrams

The phase diagrams of figure 7(d) cover R_2 - R_1 regions in which the SPI bifurcation thresholds for different M do not intersect. This ensures that any MCS branch starts and ends in the *same* SPI solution. SPIs bifurcate out of CCFs, indicated by the orange and red triangles that are approximated by solid or dashed lines to guide the eyes. Solid (dashed) lines indicate

bifurcation thresholds of stable (unstable) states⁴. Squares represent secondarily (mostly unstably) bifurcating MCSs that become stable in the hatched regions.

The simplest behaviour is observed for L3R5-MCS, which bifurcate as unstable solutions out of unstable L3-SPI and remain unstable in the whole parameter range covered in figure 7(d2). In contrast to that, L3R4-MCS and L4R5-MCS are partially stable. In figure 7(d1), the L3R4-MCSs always bifurcate as an unstable solution out of the unstable L3-SPI and later become stable in the hatched region. This region is an approximation to the simulated data points (maroon squares). The sophisticated mechanism of this stability transfer involves further states and is subject to further investigations. The L4R5-MCSs in figure 7(d3) bifurcate for (i) moderate R_2 as a stable and (ii) for larger $|R_2|$ as an unstable solution out of the unstable (i) or stable (ii) L4-SPI. The coincidence of stable L4-SPI (orange hatched region) and stably bifurcating L4R5-MCS (maroon hatched region) in figure 7(d3) is evident. Finally, figures 7(d1)–(d3) exhibit the coexistence of 3-, 4- and 5-SPI and the bistability of L3R4- and L4R5-MCS.

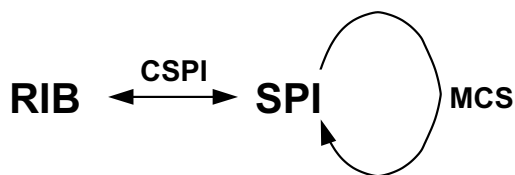
Remark. The bifurcation thresholds of, say, L3-SPI and R5-SPI intersect for a certain $R_1 > 200$. This alters the sequence of bifurcations in the sense that one finds a continuous transition from L3-SPI to R5-SPI via an MCS structure with varying spiral contributions. Under a continuous variation of the control parameters while following the entire MCS solution branch, an L3R5-MCS with a major L3 and a minor R5 component first bifurcates out of the L3-SPI. Then, it changes its shape to an MRIB with equal contributions of both components and finally to an R5L3-MCS with a major R5 and a minor L3 component. The R5L3-MCS then merges into the R5-SPI state.

5. Summary

The transition between (different) spiral states (SPIs) with the same axial wave number $k = 3.927$ is shown to be mediated by secondarily bifurcating MCSs. ‘Classical’ cross-spirals (CSPIs), on the other hand, connect SPI and RIB solutions.

Both MCSs and CSPIs can be seen as nonlinear superpositions of oppositely travelling spirals with continuously varying contributions. CSPIs consist of two *mirror-symmetric* SPIs, whereas MCSs in general consist of components corresponding to SPIs with *different* azimuthal wave numbers. Thus, CSPIs (RIBs) represent a special type of MCS (MRIB). Furthermore, RIBs (MRIBs) can be seen as a special type of CSPI (MCS) with equal amplitude contributions from L-SPI and R-SPI.

In contrast to CSPIs, which offer a way for a transition from a spiral branch back to the same branch via ribbons, the MCS solutions discussed in this paper exhibit a *direct* way for such transitions without involving further primary bifurcating solutions like RIBs or MRIBs.



⁴ Although all SPI bifurcation thresholds are R/L-symmetry degenerated, we labelled them according to the major and minor spiral component in the respective MCS solution.

Up to now, we were not able to determine complete primary bifurcating MRIB branches because they only occur in the transitions between SPIs with different helicity and different azimuthal wave number.

MCS frequencies are determined by the major spiral component, while the smaller, minor spiral component causes a modulation that propagates into the opposite direction. Thus, the spatiotemporal properties of MCSs are similar to those of pure spirals with a slight modulation. On the other hand, wavy spirals that mediate the transition from SPI to TVF contain in their spectra a (0, 1) mode that is missing here.

Two bifurcation scenarios have been found: MCSs bifurcate as a stable (unstable) solution out of a stable (unstable) spiral branch. In the first case, the stable SPI then becomes unstable. This behaviour is completely unaffected by the stability behaviour of other solutions, like RIBs or the SPI corresponding to the minor spiral component in the MCSs.

The MCSs presented in this paper always coexist simultaneously with *both* corresponding pure SPI types. This condition is not necessarily required in general since the minor component is not topologically connected to its pure spiral. For control parameters other than those discussed here, we also found MCS branches that at least partly coexist only with the pure SPIs corresponding to the major spiral component, especially in the case of MCSs that connect *different* SPI types, which will be the subject of further investigations.

The occurrence of MCSs, particularly those mediating transitions between SPIs with *different* azimuthal wave numbers M , seems to be a consequence of the periodic boundary conditions, which, in contrast to rigid axial lids, allow for multi-stable SPI solutions with different M and also for the multi-stability of different MCSs. Due to wave number selection effects in longer axial periodic systems, multi-stability regions seem to disappear mostly and it is an open question whether such regions then exist at all.

Acknowledgment

We thank the Deutsche Forschungsgemeinschaft for support.

References

- [1] DiPrima R C and Swinney H L 1985 *Hydrodynamic Instabilities and the Transition to Turbulence (Topics in Applied Physics)* ed Swinney H L and Gollub J G (Berlin: Springer)
- [2] Andereck C D, Liu S S and Swinney H L 1986 *J. Fluid Mech.* **164** 155
- [3] Langford W F *et al* 1988 *Phys. Fluids* **31** 776
- [4] Tagg R 1994 *Nonlinear Sci. Today* **4** 1
- [5] Lopez J M and Marques F 1997 *J. Fluid Mech.* **348** 153
- [6] Marques F and Lopez J M 2000 *Physica D* **136** 340
- [7] Hoffmann Ch and Lücke M 2000 *Physics of Rotating Fluids* 549 (Berlin: Springer) 55
- [8] Marques F and Lopez J M 2002 *Theor. Comput. Fluid Dyn.* **16** 59
- [9] Hoffmann Ch, Lücke M and Pinter A 2005 *Phys. Rev. E* **72** 056311
- [10] Hoffmann Ch, Lücke M and Pinter A 2004 *Phys. Rev. E* **69** 056309
- [11] Pinter A, Lücke M and Hoffmann Ch 2006 *Phys. Rev. Lett.* **96** 044506
- [12] Pinter A, Lücke M and Hoffmann Ch 2007 *Phys. Rev. E* **76** 015301
- [13] Pinter A, Lücke M and Hoffmann Ch 2008 *Phys. Rev. E* **78** 017303
- [14] Pinter A, Lücke M and Hoffmann Ch 2008 *Phys. Rev. E* **78** 015304
- [15] Tagg R, Edwards W S, Swinney H L and Marcus P S 1989 *Phys. Rev. A* **39** 3734

- [16] Chossat P and Iooss G 1994 *The Couette–Taylor Problem* (New York: Springer)
- [17] Hoffmann Ch, Altmeyer S and Lücke M 2009 *New J. Phys.* **11** 053002
- [18] Swift J W, Gorman M and Swinney H L 1982 *Phys. Lett. A* **87** 457
- [19] Swinney H L and Gollub J P 1981 *Hydrodynamic Instabilities and the Transition to Turbulence* (Berlin: Springer)
- [20] Golubitsky M, Stewart I and Schaeffer D 1988 *Singularities and Groups in Bifurcation Theory II* (New York: Springer) 485–512
- [21] Golubitsky M and Langford W F 1988 *Physica D* **32** 362
- [22] Hoffmann Ch 1998 Stationäre und zeitabhängige Strömungsmuster im Taylor–Couette System *Diploma Thesis* Universität des Saarlandes